Resolving Space Plasma Species With Electrostatic Analyzers

Georgios Nicolaou *, Richard P. Haythornthwaite and Andrew J. Coates

Mullard Space Science Laboratory, Department of Space and Climate Physics, University College London, Dorking, United Kingdom

Electrostatic analyzers resolve the energy-per-charge distributions of charged plasma particles. Some space plasma instruments use electrostatic analyzers among other units, such as aperture deflectors and position sensitive detectors, in order to resolve the three-dimensional energy (velocity) distribution functions of plasma particles. When these instruments do not comprise a mass analyzer unit, different species can be resolved only if there are measurable differences in their energy-per-charge distributions. This study examines the ability of single electrostatic analyzer systems in resolving co-moving plasma species with different mass-per-charge ratios. We consider examples of static plasma consisting of two species of heavy negative ions measured by a typical electrostatic analyzer design, similar to the electron spectrometer on board Cassini spacecraft. We demonstrate an appropriate modeling technique to simulate the basic features of the instrument response in the specific plasma conditions and we quantify its ability to resolve the key species as a function of the spacecraft speed and the plasma temperature. We show that for the parameter range we examine, the mass resolution increases with increasing spacecraft speed and decreasing plasma temperature. We also demonstrate how our model can analyze real measurements and drive future instrument designs.

Keywords: plasma physics, instrumentation, planetary physics, Methods, plasma modeling

1 INTRODUCTION

The analysis of *in-situ* plasma observations is almost always necessary in understanding the physical mechanisms in space. Ideally, space plasma observations allow the accurate determination of the distributions of plasma particle velocities, known as the velocity distribution functions (VDFs) of the plasma species. Further analysis of the plasma VDFs is crucial for the investigation of dynamical processes in plasmas, such as plasma heating and acceleration.

Top-hat electrostatic analyzers have been widely used for *in-situ* plasma observations. In principle, these analyzers resolve the energy-per-charge distributions of plasma ions or/and electrons, in directions covered by the instrument's field of view. In some applications, electrostatic analyzers resolve the entire energy-per-charge and direction range of the plasma particles, allowing the determination of the three-dimensional (3D) VDFs of plasma particles. This is achieved by combining position sensitive detectors and aperture deflectors (e.g., McComas et al., 2013; Pollock et al., 2016; Owen et al., 2020), or by being mounted on a spinning spacecraft (e.g., McComas et al., 2008) or on a motor-driven actuator (e.g., Young et al., 2004). Some instruments comprise mass analyzer units in order to distinct plasma species with different mass-per-charge (e.g., Nilsson et al., 2007; Barabash et al., 2006; Barabash et al., 2007; Johnstone et al., 1997; McComas et al., 2013).

FIGURE 1 | Schematic of the concept instrument. **(A)** The top-hat electrostatic analyzer diagram showing the narrow field of view of the elevation direction, the trajectory of a charged particle through the instrument, and the position sensitive detector. The black arrow on the bottom indicates the spacecraft's velocity direction. **(B)** View from the top of the eight azimuth anodes which resolve the azimuth direction of the detected particles.

Electrostatic analyzers without a mass analyzer unit, can still resolve different plasma species from apparent differences in the constructed energy-per-charge distributions. For example, we can often distinguish co-moving protons and alpha particles in the solar wind, in energy-per-charge spectra obtained by electrostatic analyzers (e.g., Nilsson et al., 2007; Ebert et al., 2010; Nicolaou et al., 2014a). In these cases, both species have the same bulk velocity magnitude V and direction. The bulk (mean) kinetic energy-per-charge of protons with mass m_p and charge q_p, is $\frac{E_p}{q_p} = \frac{1}{2}\frac{m_p}{q_p}V^2$ and the bulk kinetic energy-per-charge of alpha particles with mass m_a and charge q_a is $\frac{E_a}{q_a} = \frac{1}{2}\frac{m_a}{q_a}V^2$. Therefore, in the cold solar wind, the ratio of the energy-per-charge peaks for the two species is $r = 2$ (e.g., Louarn et al., 2021). However, the two peaks are not easily resolved in a hotter and/or slower solar wind plasma, because for instance at low speeds, thermal and mean ion energies become comparable (e.g., Heelis and Hanson 1998; Crary et al., 2009; Mandt et al., 2012; Nicolaou et al., 2014c).

In another example, observations by the electron spectrometer of Cassini Plasma Spectrometer (CAPS/ELS, Young et al., 2004) allow the detection of heavy negative ions in the vicinity of Titan (e.g., Coates et al., 2007; Desai et al., 2017; Wellbrock et al., 2013; Wellbrock et al., 2019) and Enceladus plume (e.g., Coates et al., 2010; Haythornthwaite et al., 2020). In these cases, the heavy ion plasma is quasi-static and the bulk velocity of the ions in the spacecraft frame is the spacecraft ram speed, therefore, it is the same for all plasma species. As a result, we can occasionally distinguish species with different mass-per-charge from distinct peaks in the energy-per-charge distribution obtained by the analyzer. However, the achieved mass resolution is a function of the spacecraft speed and the ion temperature. It is then useful to quantify the achieved mass resolution in order to prepare future plasma missions based on specific science requirements. Usually, an instrument's performance is tested using forward modeling (e.g., Nicolaou et al., 2014a; b; Nicolaou et al., 2014c; Nicolaou et al., 2014b; b, Nicolaou et al., 2020a).

In this paper, we model the response of an electrostatic analyzer in plasmas of heavy negative ions. We analyze the modeled energy-per-charge distributions recorded from the concept instrument in order to quantify the achieved mass resolution as a function of the spacecraft speed and the plasma temperature. In **Section 2**, we describe the methods we use to simulate the instrument's response and how we analyze the simulated observations. In **Section 3**, we present our model results, while in **Section 4**, we test and demonstrate the application of our model in reproducing flight observations of heavy ions in the plume of Enceladus. Finally, we discuss our findings in **Section 5**.

2 METHODOLOGY

2.1 Instrument Concept
We consider a typical top-hat electrostatic analyzer system design, similar to the CAPS/ELS on board Cassini (Young et al., 2004). **Figure 1** shows a diagram of our concept instrument. The top-hat plane lies onto the x-y plane, with the *x*-axis pointing towards the opposite direction of the spacecraft ram velocity. The *z*-axis is perpendicular to the top-hat plane and aligned with the symmetry axis of the instrument, completing the right-handed orthogonal reference frame. The energy range of our concept instrument spans from 0.58 eV to 26 keV and is covered in 64 logarithmically spaced steps E. The energy acceptance bandwidth for each energy step is $\frac{\Delta E}{E} \sim \Delta \ln E \sim 17\%$. We define the elevation angle of the flow θ as the angle between the particle velocity vector and the top-hat plane, increasing towards *z*-axis. In this study, we consider an aperture along the top hat plane which captures particles with elevation angle ranging roughly from −10° to 10°, with the response having a peak at −0.5° and full width at half maximum FWHM ~8° (see **Figure 2**). The azimuth direction ϕ is defined as the angle between the projection of the particle velocity vector on the x-y plane and the *x*-axis, increasing towards *y*-axis. The instrument captures the azimuth field-of-view (FOV) by using eight anodes on the position sensitive detector (i.e., a micro-channel-plate), lying onto the x-y plane. Each anode covers 20° (FWHM of the azimuth response), resulting in an azimuth FOV of 160°. For each energy E, the position sensitive detector resolves the azimuth direction simultaneously.
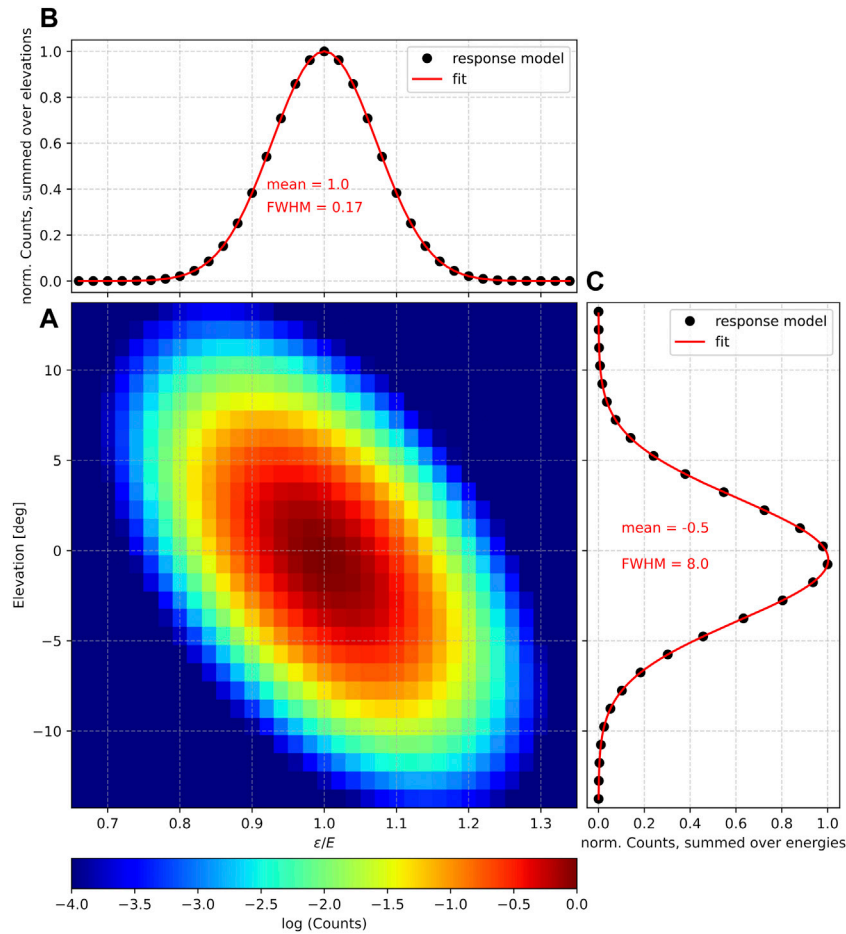
FIGURE 2 | Response function of our instrument model. **(A)** 2D response matrix showing the logarithm of the normalized particle transmission, as a function of the particle elevation direction and as a function the particle energy over the energy setting (ε/E). **(B)** The instrument transmission, integrated over elevation directions, as a function of particle ε/E and **(C)** the instrument transmission, integrated over particle ε/E, as a function of the elevation direction. The curves we show are normalized to their maximum value.

2.2 Simulated Observations

We first consider static plasma, consisting of OH$^-$ and H$_2$O-OH$^-$, similar to the negative ion plasma in the plumes of Enceladus as observed by the plasma instruments on Cassini (e.g., Coates et al., 2010). The bulk velocity of the plasma particles on the instrument frame is V_{sc}, resulting from the spacecraft ram motion through the plasma. We further assume that both species have the same number density n and temperature T. We model the velocity (energy) distribution function of the plasma, assuming Maxwellian distributions for both species, as these distributions have been used successfully in the past to describe the plasma in the Saturn's magnetosphere and moons (e.g., Crary et al., 2009; Livi et al., 2014; Desai et al., 2017). Thus, the velocity distribution for OH$^-$ ions is
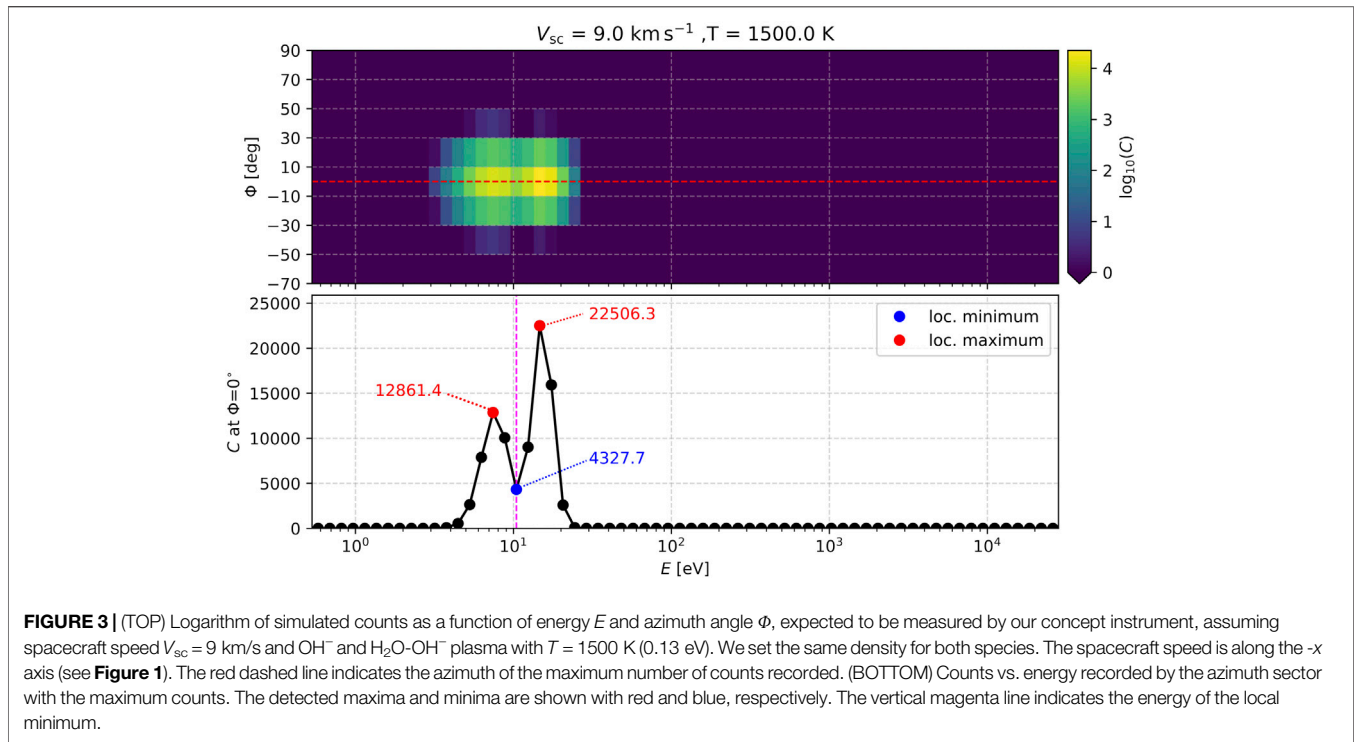
$$f_{\mathrm{OH}^-}\left(\varepsilon, \theta, \phi\right) = n\left(\frac{\mathrm{m}_{\mathrm{OH}^-}}{2\pi \mathrm{k}_\mathrm{B} T}\right)^{3/2} e^{-\left\{\frac{\mathrm{m}_{\mathrm{OH}^-}\left[v_{\mathrm{OH}^-}\left(\varepsilon,\theta,\phi\right)-V_{sc}\right]^2}{2\mathrm{k}_\mathrm{B} T}\right\}}, \quad (1)$$

and for H$_2$O-OH$^-$ ions is

$$f_{\mathrm{H_2O\text{-}OH}^-}\left(\varepsilon, \theta, \phi\right) = n\left(\frac{\mathrm{m}_{\mathrm{H_2O\text{-}OH}^-}}{2\pi \mathrm{k}_\mathrm{B} T}\right)^{3/2} e^{-\left\{\frac{\mathrm{m}_{\mathrm{H_2O\text{-}OH}^-}\left[v_{\mathrm{H_2O\text{-}OH}^-}\left(\varepsilon,\theta,\phi\right)-V_{sc}\right]^2}{2\mathrm{k}_\mathrm{B} T}\right\}}.$$

$$(2)$$

In the equations above, k_B is the Boltzmann constant, m is the ion mass, v denotes the velocity vector of the plasma particles, while subscripts denote the species.

We then calculate the expected (average) counts C to be measured at each energy E step and azimuth anode Φ of the instrument. Note that E, Φ are the energy and azimuth direction values at the center of the ε, ϕ range covered in each energy step and azimuth anode of the instrument, respectively. The instrument does not scan the elevation direction of the particles, but instead accepts particles within an elevation direction range extending above and below the top-hat plane ($\Theta = 0°$). Then, we calculate the

FIGURE 3 | (TOP) Logarithm of simulated counts as a function of energy E and azimuth angle Φ, expected to be measured by our concept instrument, assuming spacecraft speed V_{sc} = 9 km/s and OH^- and $H_2O\text{-}OH^-$ plasma with T = 1500 K (0.13 eV). We set the same density for both species. The spacecraft speed is along the $-x$ axis (see **Figure 1**). The red dashed line indicates the azimuth of the maximum number of counts recorded. (BOTTOM) Counts vs. energy recorded by the azimuth sector with the maximum counts. The detected maxima and minima are shown with red and blue, respectively. The vertical magenta line indicates the energy of the local minimum.

expected counts in each energy step E, and azimuth anode Φ as

$$
C(E, \Phi) = \frac{2}{m_{OH^-}^2} A_{eff}(E, \Phi) \Delta\tau \int_{E-\frac{1}{2}\Delta E}^{E+\frac{1}{2}\Delta E} \int_{-\frac{1}{2}\Delta\Theta}^{+\frac{1}{2}\Delta\Theta}
$$

$$
\int_{\Phi-\frac{1}{2}\Delta\Phi}^{\Phi+\frac{1}{2}\Delta\Phi} R(\varepsilon, \theta, \phi) f_{OH^-}(\varepsilon, \theta, \phi) \varepsilon d\varepsilon \cos\theta d\theta d\phi
$$

$$
+ \frac{2}{m_{H_2O-OH^-}^2} A_{eff}(E, \Phi) \Delta\tau \int_{E-\frac{1}{2}\Delta E}^{E+\frac{1}{2}\Delta E} \int_{-\frac{1}{2}\Delta\Theta}^{+\frac{1}{2}\Delta\Theta}
$$

$$
\int_{\Phi-\frac{1}{2}\Delta\Phi}^{\Phi+\frac{1}{2}\Delta\Phi} R(\varepsilon, \theta, \phi) f_{H_2O-OH^-}(\varepsilon, \theta, \phi) \varepsilon d\varepsilon \cos\theta d\theta d\phi, \quad (3)
$$

Where A_{eff} is the instrument's effective aperture which depends on both its geometry and electronic detection efficiency, and $\Delta\tau$ is the measurement acquisition time. The integral ranges over the energy acceptance bandwidth ΔE of each energy step E, the elevation angle acceptance bandwidth $\Delta\Theta$, and the azimuth angle acceptance bandwidth $\Delta\Phi$ of each azimuth sector Φ. The function $R(\varepsilon, \theta, \phi)$ is the response (transmission) function of the instrument for each energy setting E and azimuth sector Φ. We consider the energy-elevation response shown in **Figure 2A**, which is similar to the energy-elevation response of CAPS/ELS. **Figure 2B** shows the integrated over elevation response as a function of the particle energy over the energy step of the analyzer (ε/E). **Figure 2C** shows the integrated over energy response as a function of elevation angle. Furthermore, we consider a Gaussian response as a function of ϕ having a peak at the center of the azimuth sector range Φ. In the top panel of **Figure 3**, we show simulated observations $\log_{10}[C(E, \Phi)]$ for T = 1500 K (~0.13 eV) and V_{sc} = 9 km/s.

As expected, anode 4, which captures the Φ = 0° direction (anti-ram) records the largest number of counts.

2.3 Simulated Data Analysis

We detect the local maxima and minima (if any) of the simulated counts as a function of energy, obtained at the azimuth sector which observes the anti-ram direction of the spacecraft (Φ = 0°), therefore, the maximum flux. In the bottom panel of **Figure 3**, we show the expected $C(E, \Phi = 0°)$ for T = 1500 K (~ 0.13 eV) and V_{sc} = 9 km/s. We show the detected local minimum with blue, and the corresponding energy with the vertical magenta line. We also show the detected local maxima with red. To quantify the separation of the mass peaks, we calculate the difference between the smaller local maximum and the local minimum, and we normalize to the value of the local minimum. For instance, the smaller maximum in the example shown in **Figure 3** is 12,861.4 counts and the local minimum is 4,327.7 counts. The relative peak-minimum difference in this case is $\frac{peak-minimum}{minimum} = \frac{12861.4-4327.7}{4327.7} \sim 2$. It is then expected that the calculated relative peak-minimum difference increases with increasing mass resolution. In cases when there is no local maxima and a local minimum in $C(E, \Phi = 0)$ we set the peak separation at 0.

3 MODEL RESULTS

In **Figure 4**, we show examples of $C(E, \Phi = 0°)$ for different combinations of V_{sc} and plasma T. We use the same format as in the bottom panel of **Figure 3**; if $C(E, \Phi = 0°)$ has a local minimum, we indicate it with blue and we show the two local
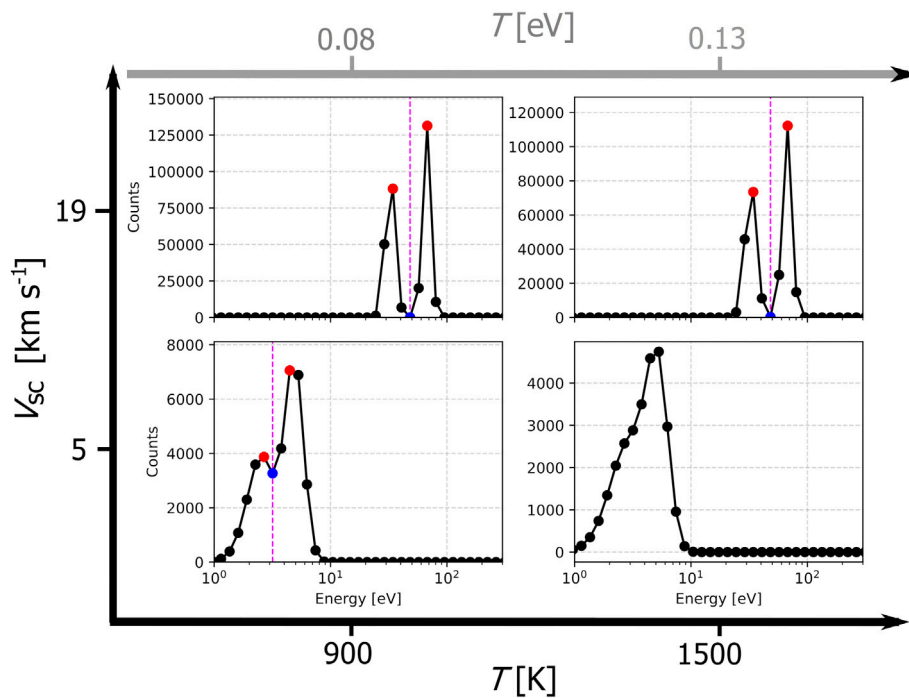
FIGURE 4 | Modeled average (expected) counts per energy for the azimuth sector $\Phi = 0°$, which records the maximum number of counts, for different spacecraft velocities and plasma temperatures. If the curve has a local minimum, we indicate it with a blue data-point and its energy is shown with the magenta line. For the same cases we show local maxima with red.
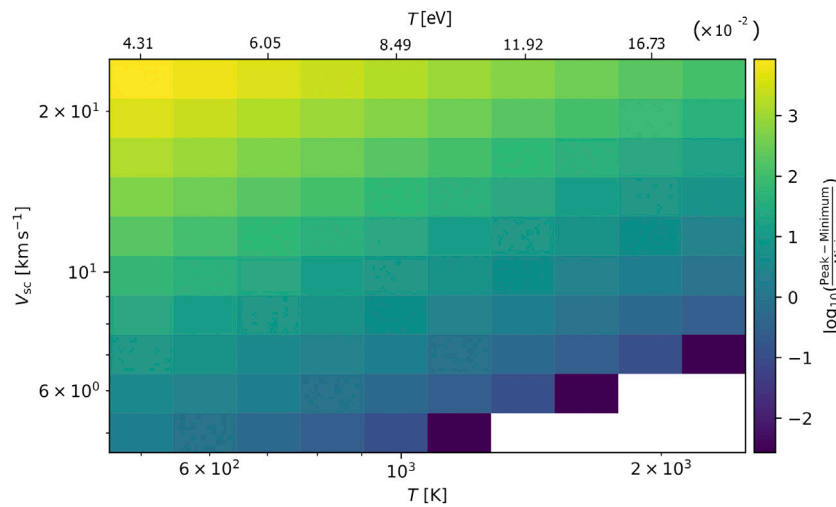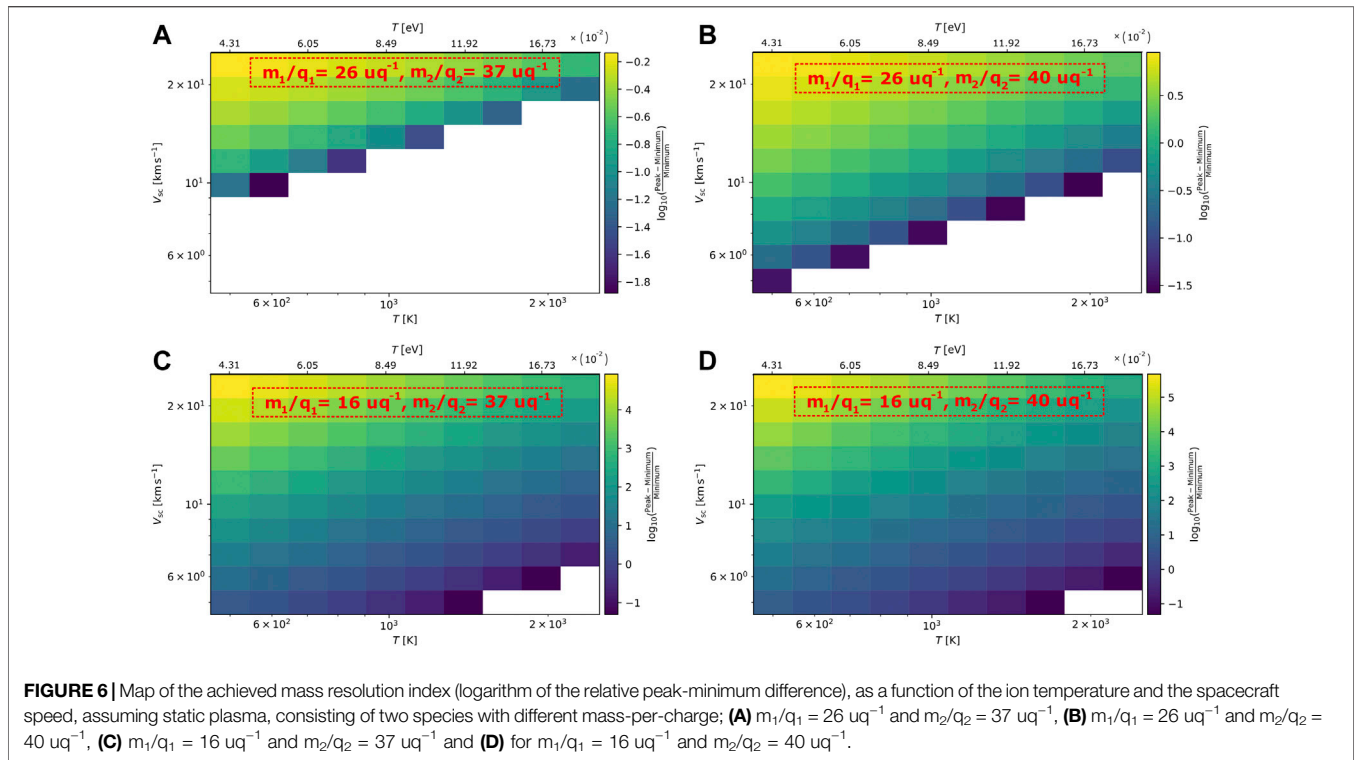

FIGURE 5 | Map of the achieved mass resolution index we use in this study (see **Section 2.3**), as a function of the ion temperature and the spacecraft speed, assuming static plasma, consisting of OH^- and $H_2O\text{-}OH^-$. The mass resolution increases with increasing spacecraft speed and decreasing plasma temperature.

maxima with red. We observe that the separation of the two peaks is more prominent (larger relative difference between minimum and maximum) with increasing spacecraft speed and decreasing plasma temperature. We also show a case of $C(E, \Phi = 0°)$ without a local minimum (bottom right panel in **Figure 4**). Although our study does not quantify a mass

resolution for such cases, a proper fitting could determine the two populations (e.g., Livi et al., 2014). However, the evaluation of such analysis is beyond the scope of this paper.

In **Figure 5**, we show the logarithm of the relative peak-minimum difference we calculate as explained in **Section 2.3**, for

FIGURE 6 | Map of the achieved mass resolution index (logarithm of the relative peak-minimum difference), as a function of the ion temperature and the spacecraft speed, assuming static plasma, consisting of two species with different mass-per-charge; **(A)** $m_1/q_1 = 26$ uq^{-1} and $m_2/q_2 = 37$ uq^{-1}, **(B)** $m_1/q_1 = 26$ uq^{-1} and $m_2/q_2 = 40$ uq^{-1}, **(C)** $m_1/q_1 = 16$ uq^{-1} and $m_2/q_2 = 37$ uq^{-1} and **(D)** for $m_1/q_1 = 16$ uq^{-1} and $m_2/q_2 = 40$ uq^{-1}.

a range of spacecraft speeds and plasma temperatures. The plot confirms that the two peaks get more prominent as the spacecraft speed increases and/or as the temperature of the two species decreases. The white color on the plot corresponds to V_{sc}—T combinations for which $C(E, \Phi = 0°)$ has no local minimum, therefore, no two distinct peaks. For the range of V_{sc} and T values we examine here, the largest relative peak difference is almost 10^4. Our instrument can resolve the two ion peaks for V_{sc} as low as 5 km/s, when the temperature is smaller than 1100 K.

For completeness, we investigate the resolution capabilities for different combinations of heavy ions. In **Figure 6**, we show the logarithm of the relative peak-minimum difference, for the same range of spacecraft speeds and plasma temperatures as in **Figure 5**, for four different ion combinations. We specifically examine mass-per-charge ratios of negative ions that are proposed to be abundant in Titan's ionosphere (Coates et al., 2007). Panel (A) shows the achieved resolution for plasma consisting of two ion species one with mass-per-charge m_1/q_1 = 26 uq^{-1} and the other with $m_2/q_2 = 37$ uq^{-1}, while panel (B) shows the results for $m_1/q_1 = 26$ uq^{-1} and the other with $m_2/q_2 = 40$ uq^{-1}. Similarly, panel (C) shows the achieved resolution for $m_1/q_1 = 16$ uq^{-1} and the other with $m_2/q_2 = 37$ uq^{-1} and panel (D) for $m_1/q_1 = 16$ uq^{-1} and the other with $m_2/q_2 = 40$ uq^{-1}. As expected, we can successfully resolve plasma species in lower Vsc and higher plasma temperatures as the mass-per-charge difference of the ions species is larger [moving from panel (A) to (D)]. With our quantitative analysis we predict how sensitive is the achieved resolution on certain parameters for given plasma composition. Although our result is indicative for an ideal instrument response, more sophisticated predictions should

include statistical measurement errors and other systematic errors associated with specific sensors.

4 APPLICATION TO FLIGHT DATA

We demonstrate how our forward model reproduces observations by the Electron Spectrometer (ELS) sensor of Cassini Plasma Spectrometer (CAPS, Young et al., 2004). The instrument observed fluxes of negative ions in the Enceladus plumes during the Enceladus encounters in 2008 (Coates et al., 2010). The analysis of the observations revealed the abundance of water group negative ions (Haythornthwaite et al., 2020). In **Figure 7**, we show ELS observations during the Cassini's E3 flyby, in terms of logarithm of the count rates ($C/\Delta\tau$), recorded in azimuth anode 5, as a function of energy and time. Azimuth anode 5 is one of the two azimuth anodes capturing ions flowing in the anti-ram direction of the spacecraft (within 10°). With the magenta box, we indicate a time period in which both OH$^-$ and H$_2$O-OH$^-$ ions are clearly observed. In the lower energy range (<20 eV) we observe enhanced count rates corresponding to plasma electrons e$^-$, or a mixture of e$^-$ with H$^-$ ions which cannot be distinguished. Nevertheless, in our efforts to characterize the signatures of heavy negative ions, we need to take into account that the distribution e$^-$ (or e$^-$ and H$^-$) overlaps with the distribution of OH$^-$. The high count rates in the higher energy range (> 200 eV) correspond to charged dust (Jones et al., 2009; Hill et al., 2012), which is not expected to play any role in our analysis, as it does not have a significant overlap with the distribution of heavy negative ions we examine here.
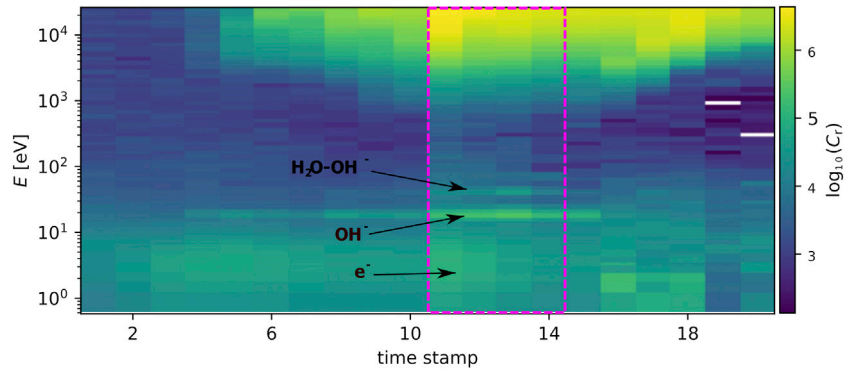
FIGURE 7 | Observations of CAPS Electron Spectrometer during the Enceladus encounter on 12-03-2008. The arrows indicate signatures of electrons, OH⁻ and H₂O-OH⁻ ions. The magenta square shows a time period in which both OH⁻ and H₂O-OH⁻ ions are detected within the energy-per-charge range of the instrument.
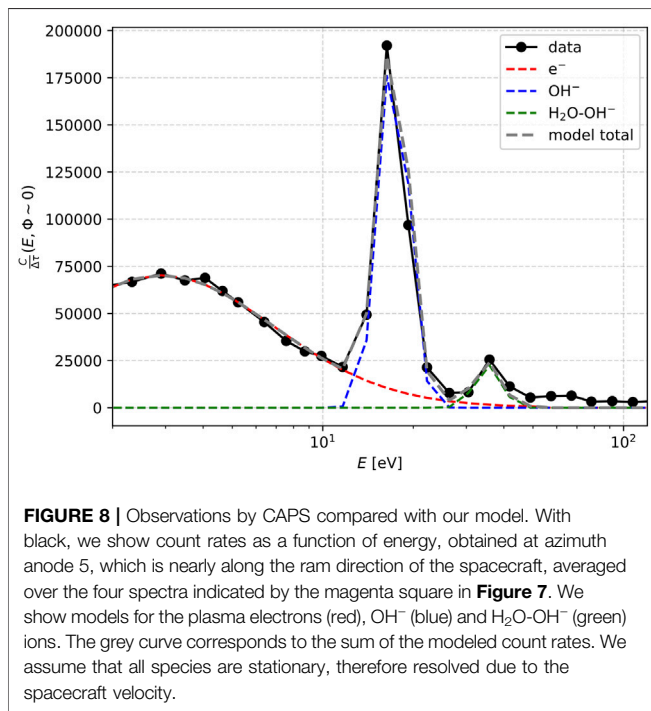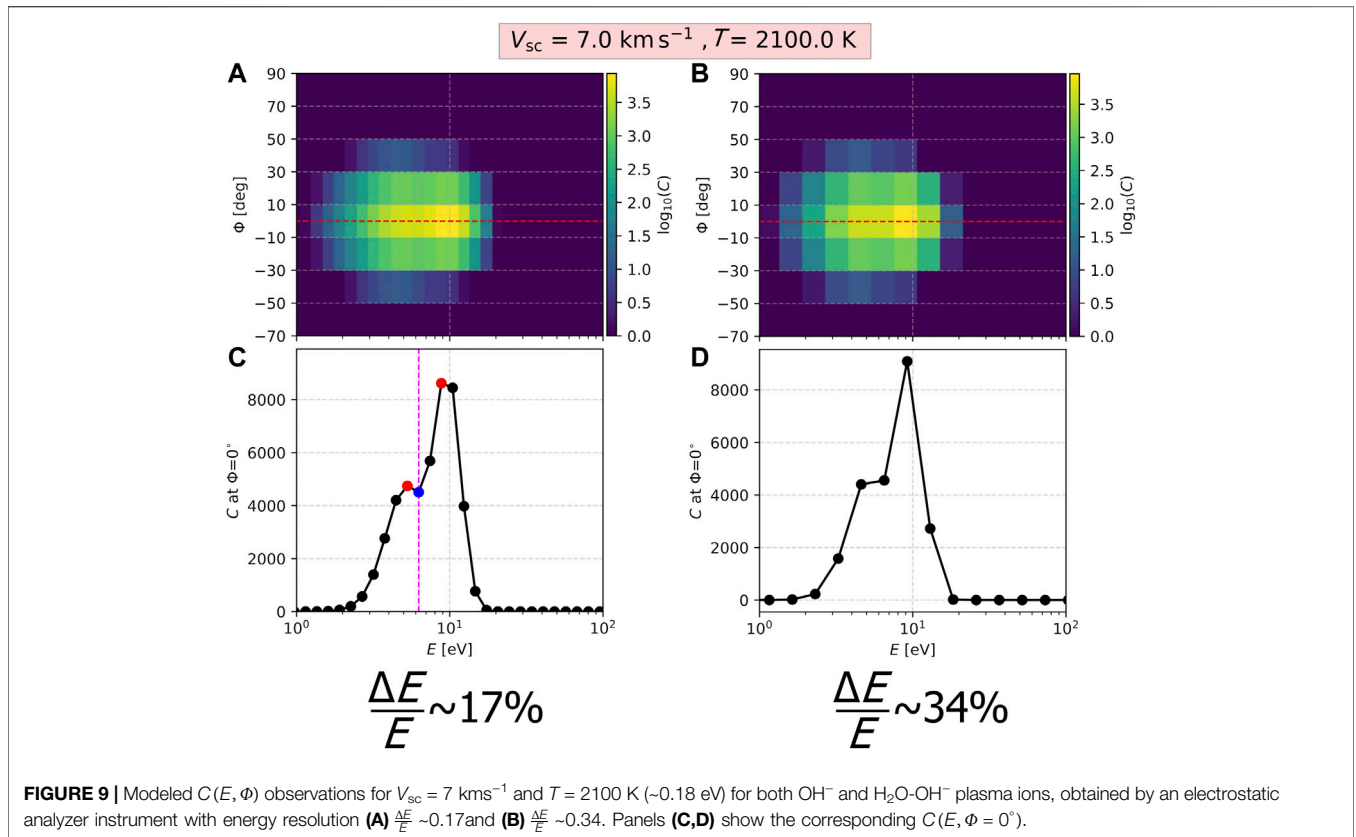

FIGURE 8 | Observations by CAPS compared with our model. With black, we show count rates as a function of energy, obtained at azimuth anode 5, which is nearly along the ram direction of the spacecraft, averaged over the four spectra indicated by the magenta square in **Figure 7**. We show models for the plasma electrons (red), OH⁻ (blue) and H₂O-OH⁻ (green) ions. The grey curve corresponds to the sum of the modeled count rates. We assume that all species are stationary, therefore resolved due to the spacecraft velocity.

In **Figure 8**, we show the averaged $(E, \Phi \sim 0)$ over the four selected spectra (black). We attempt to reproduce the observations by modeling the instrument response, as explained in **Section 2**, in the presence of plasma electrons, OH⁻ and H₂O-OH⁻ ions. The colored dashed lines in **Figure 8**, show the count rates associated with each of the modeled species, along with the total count rate resulting from all species together. We set the same velocity $V_{sc} \sim 14$ km/s to all the modeled plasma species, accounting also for the spacecraft ram direction in respect to the center of the azimuth anode. The model assumes a heavy ion density ratio $n_{OH^-}/n_{H_2O-OH^-} = 10$, $T_{OH^-} = 800$ K (~0.07 eV) and $T_{H_2O-OH^-} = 2100$ K (~0.10 eV). We finally assume that the electron velocities follow a kappa -distribution function. Our

model curve captures the basic features of the observed curve, such as the location and shape of each peak, suggesting that our model and its assumptions are reasonable. For the specific plasma parameters and spacecraft speed, the two peaks are well resolved. We finally note that we did not use a fitting routine to optimize the plasma parameters in the model we show here. A dedicated analysis to determine the plasma parameters should be performed in the future after quantifying and including all the relevant measurement errors (e.g., statistical error of measured counts and calibration errors).

5 DISCUSSION

We demonstrate the use of an appropriate forward model simulating the expected response of an electrostatic analyzer in the presence of plasma of heavy, negative ions. The development of forward models is not only useful in data-analyses (e.g., Nicolaou et al., 2014b; Nicolaou et al., 2021; Wilson et al., 2008; Wilson et al., 2017, Elliott et al., 2016), but also in testing the performance of the instrument in a range of expected conditions (Kessel et al., 1989; Cara et al., 2017; Nicolaou et al., 2014c; Nicolaou et al., 2014b; Nicolaou et al., 2020a; Nicolaou et al., 2020b; Nicolaou and Livadiotis, 2016). In this study we focus on the ability to resolve key species for plasma science in the vicinity of Enceladus and Titan. For simplicity, we investigate the achieved mass resolution assuming plasma of two species at a time, having the same density n and temperature T and that their bulk kinetic energy in the planetary frame is negligible. We then quantify the mass resolution only as a function of the spacecraft speed V_{sc} and T. Nevertheless, future studies can use the same analysis methods we use here in order to examine the achieved mass resolution for any instrument design and for a wide range of all the relevant plasma parameters (density, temperature of both species and spacecraft velocity). Our results show that the achieved mass resolution is improved with increasing spacecraft speed and decreasing temperature of the plasma species.

FIGURE 9 | Modeled $C(E, \Phi)$ observations for V_{sc} = 7 kms^{-1} and T = 2100 K (~0.18 eV) for both OH$^-$ and H$_2$O-OH$^-$ plasma ions, obtained by an electrostatic analyzer instrument with energy resolution **(A)** $\frac{\Delta E}{E}$ ~0.17and **(B)** $\frac{\Delta E}{E}$ ~0.34. Panels **(C,D)** show the corresponding $C(E, \Phi = 0°)$.

The mass resolution depends on the shape of the measured counts over the energy-per-charge range of the instrument, which depends on the shape of the VDF and the mass of the ions. In our case, the total number of counts is the sum of the two detected species we consider in each example. The $C(E, \Phi = 0°)$ curve of each species has one peak, and a certain width around the peak, depending on the bulk speed of the ions and their temperature. Here, we define the mass resolution as the ability to distinguish the two species curves in the total counts curve. Therefore, the mass resolution increases as the number of energy bins between the two peaks increases (two peaks are further apart), and as the width of the curve around the peaks gets smaller. As discussed extensively in Nicolaou and Livadiotis, 2016, the location of the $C(E, \Phi = 0°)$ peaks for individual species is a function of both the bulk speed and the plasma temperature. However, when the bulk speed is considerably larger than the thermal speed, the peaks appear at $E_{peak} = E_{bulk} = \frac{1}{2}m_s V_{bulk}^2$. In our case, $V_{bulk} = V_{sc}$, so $E_{peak} = \frac{1}{2}m_s V_{sc}^2$, where the subscript "s" denotes the ions species. As a result, the energy difference of the two mass peaks increases with increasing bulk speed. On the other hand, the width of the curve around the peaks increases (the mass resolution decreases), with increasing temperature, since by definition, the temperature is analogous to the spread of the particle velocities (energies), as can be seen in **Eqs. 1**, **2**. We note however, that in the general case when flow speed V_{flow} of any of the plasma species is not negligible compared to V_{sc},

then it will become a crucial factor in the achieved mass resolution as it will shift the location of the peaks. In such a case the bulk speed in the instrument frame is $V_{bulk} = V_{sc} + V_{flow}$, so $E_{peak} = \frac{1}{2}m_s (V_{sc} + V_{flow})^2$ (e.g., Heelis and Hanson, 1998; Crary et al., 2009). As a rule of thumb then, the mass resolution decreases for increasing flow speed of the light ions and increases for increasing flow speed of the heavy ions.

By the definition of the plasma kinetic energy, we expect that the energy resolution of the analyzer is directly related to the achieved mass resolution. We would also like to discuss briefly, how the instrument's energy resolution drives the achieved mass resolution, considering the same spacecraft speed and plasma temperature. We assume OH$^-$ and H$_2$O-OH$^-$ plasma of T = 2100 K, measured by an electrostatic analyzer on a spacecraft moving with V_{sc} = 7 kms^{-1}. We model the expected observations $C(E, \Phi = 0°)$ using the instrument we use through this paper, which scans the energy range in 64 steps, resulting in an energy resolution $\frac{\Delta E}{E}$ ~ 17%. We then repeat the observations of the same plasma, considering an instrument that scans the same energy range in 32 steps, resulting to $\frac{\Delta E}{E}$ ~ 34%. **Figure 9** shows our model predictions. The two peaks are clearly distinct in the measurements of the first design, but as we decrease the energy resolution for the second model, the two peaks are lost. This exercise should be done when designing instruments based on specific scientific requirements. We note however, that the energy resolution of an

electrostatic analyzer is increased by reducing the space between the analyzer domes, effectively decreasing the instrument's aperture. As a result, the instrument measures a smaller number of counts for the same plasma conditions, reducing the statistical significance of the observations. The use of forward models like the one we demonstrate here, can predict the performance of different instrument designs and optimize the instrument characteristics that result to the best balance between resolution and efficiency.

Finally, in **Section 4**, we attempted to reproduce observations with clear signatures of heavy negative ions by the electron spectrometer of CAPS on board Cassini. By adjusting the ion bulk parameters, we achieved a good agreement between the model and the observations. This is an encouraging result indicating that our model is not only useful in predicting the performance of current and future instrument designs, but is also appropriate for further dedicated, scientific analysis of existing observations. However, for our demonstration here, we average four spectra together and we ignore the statistical measurement errors. We simplify further by assuming an ideal instrument response and ignoring effects due to spacecraft charging. For a future scientific analysis of the observations, we could develop a fitting algorithm that optimizes the plasma parameters for each spectrum separately, considering the detailed instrument calibration and including spacecraft potential effects which affect the location of the measured peaks (e.g., Anderson et al., 1994; Heelis and Hanson 1998; Bergman et al., 2020). Also, we should consider the statistical measurement error in our evaluation, in cases when the detected number of particles is low. Finally, for generalizing the model in future applications for other plasma environments, we can use different plasma velocity distribution functions, such as kappa distributions (e.g., Livadiotis and McComas, 2013 and references therein).

DATA AVAILABILITY STATEMENT

The datasets presented in this study can be found in online repositories. For this study, we analyzed Cassini CAPS data which are available from the NASA PDS (http://pds.nasa.gov/).

AUTHOR CONTRIBUTIONS

GN led the data analysis, simulations and paper writing. RH advised on the data analysis and provided useful information and resources. AC provided useful information and resources. All authors read the paper and approved its submission.

FUNDING

ACKNOWLEDGMENTS

REFERENCES

Anderson, P. C., Hanson, W. B., Coley, W. R., and Hoegy, W. R. (1994). Spacecraft Potential Effects on the Dynamics Explorer 2 Satellite. *J. Geophys. Res.* 99 (A3), 3985–3997. doi:10.1029/93JA02104

Barabash, S., Lundin, R., Andersson, H., Brinkfeldt, K., Grigoriev, A., Gunnel, H., et al. (2006). The Analyzer of Space Plasmas and Energetic Atoms (ASPERA-3) for the Mars Express Mission. *Space Sci. Rev.* 126, 113–164. doi:10.1007/s11214-006-9124-8

Barabash, S., Sauvaud, J.-A., Gunell, H., Andersson, H., Grigoriev, A., Brinkfeldt, K., et al. (2007). The Analyser of Space Plasmas and Energetic Atoms (ASPERA-4) for the Venus Express Mission. *Planet. Space Sci.* 55, 1772–1792. doi:10.1016/j.pss.2007.01.014

Bergman, S., Stenberg Wieser, G., Wieser, M., Johansson, F. L., and Eriksson, A. (2020). The Influence of Spacecraft Charging on Low-Energy Ion Measurements Made by Rpc-Ica on Rosetta. *J. Geophys. Res. Space Phys.* 125, e2019JA027478. doi:10.1029/2019ja027478

Cara, A., Lavraud, B., Fedorov, A., De Keyser, J., DeMarco, R., Marcucci, M. F., et al. (2017). Electrostatic Analyzer Design for Solar Wind Proton Measurements with High Temporal, Energy, and Angular Resolutions. *J. Geophys. Res. Space Phys.* 122, 1439–1450. doi:10.1002/2016ja023269

Coates, A. J., Crary, F. J., Lewis, G. R., Young, D. T., Waite, J. H., and Sittler, E. C. (2007). Discovery of Heavy Negative Ions in Titan's Ionosphere. *Geophys. Res. Lett.* 34, L22103. doi:10.1029/2007GL030978

Coates, A. J., Jones, G. H., Lewis, G. R., Wellbrock, A., Young, D. T., Crary, F. J., et al. (2010). Negative Ions in the Enceladus Plume. *Icarus* 206, 618–622. doi:10.1016/j.icarus.2009.07.013

Crary, F. J., Magee, B. A., Mandt, K., Waite, J. H., Westlake, J., and Young, D. T. (2009). Heavy Ions, Temperatures and Winds in Titan's Ionosphere: Combined Cassini CAPS and INMS Observations. *Planet. Space Sci.* 57, 1847–1856. doi:10.1016/j.pss.2009.09.006

Desai, R. T., Coates, A. J., Wellbrock, A., Vuitton, V., Crary, F. J., González-Caniulef, D., et al. (2017). Carbon Chain Anions and the Growth of Complex Organic Molecules in Titan's Ionosphere. *Astrophys. J. Letters* 844, L18. doi:10.3847/2041-8213/aa7851

Ebert, R. W., McComas, D. J., Bagenal, F., and Elliott, H. A. (2010). Location, Structure, and Motion of Jupiter's Dusk Magnetospheric Boundary From ∼625 to 2550 RJ. *J. Geophys. Res.* 115, A12223. doi:10.1029/2010JA015938

Elliott, H. A., McComas, D. J., Zirnstein, E. J., Randol, B. M., Delamere, P. A., and Livadiotis, G. (2019). Slowing of the Solar Wind in the Outer Heliosphere. *Astrophys. J* 885, 156. doi:10.3847/0067-0049/223/2/19

Haythornthwaite, R. P., Coates, A. J., Jones, G. H., and Waite, J. H. (2020). Fast and Slow Water Ion Populations in the Enceladus Plume. *J. Geophys. Res. Space Phys.* 125, e2019JA027591. doi:10.1029/2019ja027591

Heelis, R. A., and Hanson, W. B. (1998). "Measurements of Thermal Ion Drift Velocity and Temperature Using Planar Sensors," in *Measurement Techniques in Space Plasmas: Particles*. Editors R. F. Pfaff, J. Borovsky, and D. T. Young. doi:10.1029/GM102p0061

Hill, T. W., Thomsen, M. F., Tokar, R. L., Coates, A. J., Lewis, G. R., Young, D. T., et al. (2012). Charged Nanograins in the Enceladus Plume. *J. Geophys. Res.* 117, A05209. doi:10.1029/2011ja017218

Johnstone, A. D., Alsop, C., Burge, S., Carter, P. J., Coates, A. J., Coker, A. J., et al. (1997). PEACE: A Plasma Electron and Current Experiment. *Space Sci. Rev.* 79, 351–398. doi:10.1007/978-94-011-5666-0_13

Jones, G. H., Arridge, C. S., Coates, A. J., Lewis, G. R., Kanani, S., Wellbrock, A., et al. (2009). Fine Jet Structure of Electrically Charged Grains in Enceladus' Plume. *Geophys. Res. Lett.* 36, L16204. doi:10.1029/2009gl038284

Kessel, R. L., Johnstone, A. D., Coates, A. J., and Gowen, R. A. (1989). Space Plasma Measurements with Ion Instruments. *Rev. Sci. Instrum.* 60, 3750–3761. doi:10.1063/1.1141075

Livadiotis, G., and McComas, D. J. (2013). Understanding Kappa Distributions: A Toolbox for Space Science and Astrophysics. *Space Sci. Rev.* 175, 183–214. doi:10.1007/s11214-013-9982-9

Livi, R., Goldstein, J., Burch, J. L., Crary, F., Rymer, A. M., Mitchell, D. G., et al. (2014). Multi-instrument Analysis of Plasma Parameters in Saturn's Equatorial, Inner Magnetosphere Using Corrections for Corrections for Spacecraft Potential and Penetrating Background Radiation. *J. Geophys. Res. Space Phys.* 119, 3683–3707. doi:10.1002/2013ja019616

Louarn, P., Fedorov, A., Prech, L., Owen, C. J., Bruno, R., Livi, S., et al. (2021). Multiscale Views of an Alfvénic Slow Solar Wind: 3D Velocity Distribution Functions Observed by the Proton-Alpha Sensor of Solar Orbiter. *A&A* 656, 10. doi:10.1051/0004-6361/202141095

Mandt, K. E., Gell, D. A., Perry, M., Hunter Waite, J., Crary, F. A., Young, D., et al. (2012). Ion Densities and Composition of Titan's Upper Atmosphere Derived from the Cassini Ion Neutral Mass Spectrometer: Analysis Methods and Comparison of Measured Ion Densities to Photochemical Model Simulations. *J. Geophys. Res.* 117, E10006. doi:10.1029/2012JE004139

McComas, D., Allegrini, F., Bagenal, F., Casey, P., Delamere, P., Demkee, D., et al. (2008). The Solar Wind Around Pluto (SWAP) Instrument Aboard *New Horizons*. *Space Sci. Rev.* 140, 261–313. doi:10.1007/s11214-007-9205-3

McComas, D. J., Alexander, N., Allegrini, F., Bagenal, F., Beebe, C., Clark, G., et al. (2013). The Jovian Auroral Distributions Experiment (JADE) on the Juno Mission to Jupiter. *Space Sci. Rev.* 213, 547–643. doi:10.1007/s11214-013-9990-9

Nicolaou, G., and Livadiotis, G. (2016). Statistical Uncertainties of Space Plasma Properties Described by Kappa Distributions. *Entropy* 22, 541. doi:10.3390/e22050541

Nicolaou, G., McComas, D. J., Bagenal, F., and Elliott, H. A. (2014a). Properties of Plasma Ions in the Distant Jovian Magnetosheath Using Solar Wind Around Pluto Data on New Horizons. *J. Geophys. Res. Space Phys.* 119, 3463–3479. doi:10.1002/2013ja019665

Nicolaou, G., Verscharen, D., Wicks, R. T., and Owen, C. T. (2014b). The Impact of Turbulent Solar Wind Fluctuations on Solar Orbiter Plasma Proton Measurements. *Astrophys. J.* 886, 101. doi:10.3847/1538-4357/ab48e3

Nicolaou, G., Livadiotis, G., Owen, C. J., Verscharen, D., and Wicks, R. T. (2014c). Determining the Kappa Distributions of Space Plasmas from Observations in a Limited Energy Range. *Astrophys. J. Letters* 864, 3. doi:10.3847/1538-4357/aad45d

Nicolaou, G., Wicks, R., Livadiotis, G., Verscharen, D., Owen, C., and Kataria, D. (2020a). Determining the Bulk Parameters of Plasma Electrons from Pitch-Angle Distribution Measurements. *Entropy* 22, 103. doi:10.3390/e22010103

Nicolaou, G., Wicks, R. T., Rae, I. J., and Kataria, D. O. (2020b). Evaluating the Performance of a Plasma Analyzer for a Space Weather Monitor Mission Concept. *Space Weather* 18, e2020SW002559.

Nicolaou, G., Wicks, R. T., Owen, C. J., Kataria, D. O., Chandrasekhar, A., Lewis, G. R., et al. (2021). Deriving the Bulk Properties of Solar Wind Electrons Observed by Solar Orbiter. A Preliminary Study of Electron Plasma Thermodynamics. *A&A. Forthcom. Artic* 656, A31. doi:10.1051/0004-6361/202140875

Nilsson, H., Lundin, R., Lundin, K., Barabash, S., Borg, H., Norberg, O., et al. (2007). RPC-ICA: The Ion Composition Analyzer of the Rosetta Plasma Consortium. *Space Sci. Rev.* 128, 671–695. doi:10.1007/s11214-006-9031-z

Owen, C. J., Bruno, R., Livi, S., Louarn, P., Al Janabi, K., Allegrini, F., et al. (2020). The Solar Orbiter Solar Wind Analyser (SWA) Suite. *A&A* 642, A16. doi:10.1051/0004-6361/201937259

Pollock, C., Moore, T., Jacques, A., Burch, J., Gliese, U., Saito, Y., et al. (2016). Fast Plasma Investigation for Magnetospheric Multiscale. *Space Sci. Rev.* 199, 331–406. doi:10.1007/s11214-016-0245-4

Wellbrock, A., Coates, A. J., Jones, G. H., Lewis, G. R., and Waite, J. H. (2013). Cassini CAPS-ELS Observations of Negative Ions in Titan's Ionosphere: Trends of Density with Altitude. *Geophys. Res. Lett.* 40, 4481–4485. doi:10.1002/grl.50751

Wellbrock, A., Coates, A. J., Jones, G. H., Vuitton, V., Lavvas, P., Desai, R. T., et al. (2019). Heavy Negative Ion Growth in Titan's Polar Winter. *MNRAS* 490, 2254–2261. doi:10.1093/mnras/stz2655

Wilson, R. J., Bagenal, F., and Persoon, A. M. (2017). Survey of Thermal Plasma Ions in Saturn's Magnetosphere Utilizing a Forward Model. *J. Geophys. Res. Space Phys.* 122, 7256–7278. doi:10.1002/2017ja024117

Wilson, R. J., Tokar, R. L., Henderson, M. G., Hill, T. W., Thomsen, M. F., and Pontius, D. H. (2008). Cassini Plasma Spectrometer Thermal Ion Measurements in Saturn's Inner Magnetosphere. *J. Geophys. Res.* 113, A12218. doi:10.1029/2008ja013486

Young, D. T., Berthelier, J. J., Blanc, M., Burch, J. L., Coates, A. J., Goldstein, R., et al. (2004). Cassini Plasma Spectrometer Investigation. *Space Sci. Rev.* 114, 1–112. doi:10.1007/s11214-004-1406-4